Missing-in-metastasis and IRSp53 deform $PI(4,5)P_2$-rich membranes by an inverse BAR domain–like mechanism

Pieta K. Mattila, Anette Pykäläinen, Juha Saarikangas, Ville O. Paavilainen, Helena Vihinen, Eija Jokitalo, and Pekka Lappalainen

Institute of Biotechnology, University of Helsinki, 00014 Helsinki, Finland

The actin cytoskeleton plays a fundamental role in various motile and morphogenetic processes involving membrane dynamics. We show that actin-binding proteins MIM (missing-in-metastasis) and IRSp53 directly bind $PI(4,5)P_2$-rich membranes and deform them into tubular structures. This activity resides in the N-terminal IRSp53/MIM domain (IMD) of these proteins, which is structurally related to membrane-tubulating BAR (Bin/amphiphysin/Rvs) domains. We found that because of a difference in the geometry of the $PI(4,5)P_2$-binding site, IMDs induce a membrane curvature opposite that of BAR domains and deform membranes by binding to the interior of the tubule. This explains why IMD proteins induce plasma membrane protrusions rather than invaginations. We also provide evidence that the membrane-deforming activity of IMDs, instead of the previously proposed F-actin–bundling or GTPase-binding activities, is critical for the induction of the filopodia/microspikes in cultured mammalian cells. Together, these data reveal that interplay between actin dynamics and a novel membrane-deformation activity promotes cell motility and morphogenesis.

Introduction

The actin cytoskeleton is essential for numerous cellular and developmental processes involving membrane dynamics. These include endocytosis, cell migration, cytokinesis, and various morphogenetic processes. The polymerization, depolymerization, and 3D organization of actin filaments in cells are governed by vast number of actin-binding proteins. Most actin-binding proteins are composed of multiple domains, performing also regulatory and signaling functions. Among the plethora of actin-binding proteins are the actin filament nucleating Arp2/3 complex and its activators Wiskott-Aldrich syndrome protein (WASP) and WASP family verprolin homologous proteins (WAVEs), which promote formation of membrane protrusions downstream of the Rho-family GTPases (Pollard and Borisy, 2003). Although most actin-dependent processes involve reshaping of cellular membranes, the direct effects of actin-binding proteins on the organization of membranes has not been reported.

One central group of proteins functioning at the interface between signaling and the actin cytoskeleton are insulin receptor substrate (IRS) p53, missing-in-metastasis (MIM), and their homologues. These proteins share similar domain organization to each other, possessing a recently identified IRSp53/MIM domain (IMD) at their N terminus. In addition to the IMD, MIM and some IRSp53 isoforms possess a C-terminal WH2 domain that binds actin monomers with high affinity (Mattila et al., 2003; Woodings et al., 2003). Although the exact functions of IRSp53 and MIM are not defined, both proteins are linked to the Arp2/3-mediated actin filament assembly and formation of plasma membrane protrusions. IRSp53 interacts with the small GTPases Cdc42 and Rac through its N-terminal region and with WAVE2 through its central SH3 domain (Krugmann et al., 2001). IRSp53 regulates the Arp2/3-modulating activity of the WAVE2 complex and is involved in lamellipodia and filopodia formation in motile cells (Nakagawa et al., 2003; Suetsugu et al., 2006a). MIM was originally identified as a putative tumor suppressor because it is expressed in nonmetastatic, but absent from metastatic, bladder cancer cells (Lee et al., 2002; Loberg et al., 2005). MIM is a sonic hedgehog (Shh) responsive gene

A. Pykäläinen and J. Saarikangas contributed equally to this paper.

Correspondence to Pekka Lappalainen: pekka.lappalainen@helsinki.fi

Abbreviations used in this paper: Bar, Bin/amphiphysin/Rvs; DLS, dynamic light scattering; IMD, IRSp53/MIM domain; IRS, insulin receptor substrate; MIM, missing-in-metastasis; PC, phosphatidylcholine; PE, phosphatidylethanolamine; PS, phosphatidylserine; SPR, surface plasmon resonance; WASP, Wiskott-Aldrich syndrome protein; WAVE, WASP family verprolin homologous protein.

The online version of this article contains supplemental material.

The Journal of Cell Biology, Vol. 176, No. 7, March 26, 2007 953–964
http://www.jcb.org/cgi/doi/10.1083/jcb.200609176

and is strongly expressed during development in muscles and postmitotic neurons and in adult mice in kidneys, liver, and Purkinje cells of the cerebellum (Mattila et al., 2003; Callahan et al., 2004). MIM enhances Arp2/3-mediated actin polymerization through interactions with cortactin but inhibits WASP-mediated actin polymerization (Lin et al., 2005).

In cells, MIM and IRSp53 localize to the plasma membrane and are involved in the formation of membrane protrusions. The filopodia/membrane ruffle–inducing activity of MIM and IRSp53 resides in the N-terminal IMD, as indicated by a drastic induction of filopodia when this domain is ectopically expressed in mammalian cells (Yamagishi et al., 2004; Bompard et al., 2005). Previous studies demonstrated that recombinant IMDs bind and bundle actin filaments and interact with the small GTPase Rac, providing a plausible explanation for their filopodia-forming activity (Miki et al., 2000; Bompard et al., 2005).

The crystal structures of the IMDs from IRSp53 and MIM revealed an α-helical coiled-coil domain that self-associates into a "zeppelin-shaped" dimer (Millard et al., 2005; Lee et al., 2007). Surprisingly, the closest structural homologues of IMD are the lipid-binding BAR (Bin/amphiphysin/Rvs) domains. BAR domain proteins (e.g., amphipysin, endophilin, and Rvs161/167) and related F-BAR domain proteins (e.g., toca and syndapin) induce tubular invaginations from the plasma membrane during the formation of an endocytic vesicle (Itoh and De Camilli, 2006). In vitro, BAR domains evaginate liposomes into narrow tubules. They interact with negatively charged lipids through patches of positively charged residues at the concave face. Membrane deformation is driven by the intrinsic curvature of the rigid "banana-shaped" BAR domain dimer (Zhang and Hinshaw, 2001; Peter et al., 2004). In addition, an amphipathic N-terminal helix found in a subset of BAR domains (N-BARs) penetrates the membrane and potentiates the membrane-tubulating activity (Gallop et al., 2006; Masuda et al., 2006). In contrast to BAR domains, IMDs are involved in the formation of membrane protrusions, rather than membrane invaginations, and have not been reported to deform membranes.

Here, we provide evidence that IMDs deform $PI(4,5)P_2$-rich membranes into tubular structures. Unlike previously characterized membrane-tubulating domains, the IMD appears to bind to the inner surface of the membrane tubule and therefore promote the formation of plasma membrane protrusions rather than invaginations. Identification of the $PI(4,5)P_2$-binding interface of the IMD provided a molecular explanation for this membrane-tubulating activity and revealed how this novel function is linked to filopodia formation in cells. We also show that the filopodia-forming activity of MIM is independent of F-actin bundling and GTPase binding of the IMD.

Results

IMDs bind and deform $PI(4,5)P_2$-rich membranes

IMDs share remote structural homology with BAR domains, which bind and deform lipid membranes in vivo and in vitro (Itoh and De Camilli, 2006). Despite the structural similarity, IMDs were proposed to promote filopodia formation through their F-actin–bundling activity and thus form a functionally distinct group within the BAR domain family (Yamagishi et al., 2004; Gonzalez-Quevedo et al., 2005; Millard et al., 2005). To examine whether IMDs display a BAR domain–like membrane-binding activity, we studied the interaction of the IMD of MIM with various lipids by native gel electrophoresis. We found that it interacts with micelles containing $PI(3,4)P_2$ and $PI(4,5)P_2$ (Fig. 1 A). The polar head group of $PI(4,5)P_2$, IP_3, or other phospholipids did not shift the motility of MIM/IMD, suggesting the lack of a high-affinity interaction. The MIM/IMD–$PI(4,5)P_2$ interaction was examined further in a more physiological context with a high-speed cosedimentation assay using synthetic lipid vesicles. The IMD of MIM cosedimented with vesicles containing 30% $PI(4,5)P_2$, whereas only weak cosedimentation was detected with vesicles without $PI(4,5)P_2$ (Fig. 1 B). A more detailed analysis revealed that already 5–10% of $PI(4,5)P_2$ considerably increased the affinity of MIM/IMD to vesicles (Fig. S1, available at http://www.jcb.org/cgi/content/full/jcb.200609176/DC1). This $PI(4,5)P_2$ density is similar to the one reported for other PIP_2-interacting proteins, such as N-WASP, which requires 10–15% PIP_2 density for activation (Papayannopoulos et al., 2005). It is also important to note that, based on native gel electrophoresis (Fig. 1 A) and cosedimentation assays (Fig. S1), the IMD of MIM binds $PI(3,4,5)P_3$ with considerably lower affinity than $PI(4,5)P_2$.

Sequence database searches revealed two alternative splice variants of mouse MIM's IMD. These differ from each other by a four-amino-acid insertion encoded by exon 7 (Fig. S2, A and B, available at http://www.jcb.org/cgi/content/full/jcb.200609176/DC1). These residues are located at distal ends of the dimeric IMD (Fig. S2 C). The two alternatively spliced forms of the IMD of MIM are referred as MIM/IMD-L (longer splice variant) and MIM/IMD-S (variant lacking the four residues coded by exon 7). Importantly, both MIM/IMD-L and -S, as well as the IMD of IRSp53, interacted strongly with $PI(4,5)P_2$-containing vesicles, suggesting that $PI(4,5)P_2$ binding is a function common among all IMDs (Fig. 1 B and Fig. S3).

To investigate the possible effects of IMDs on the structure of $PI(4,5)P_2$-rich membranes, we performed an EM analysis of MIM/IMD-L–$PI(4,5)P_2$ vesicle complexes. Surprisingly, these experiments revealed a strong membrane deforming/tubulating activity. Synthetic vesicles without MIM/IMD-L were heterogeneous in size, mostly spherical or curved in shape, and evenly distributed throughout the sample. In the presence of MIM/IMD-L, these vesicles formed clusters with complex tubular structures (Fig. 1, C and D). Similar structures were also predominant in samples containing the IMD of IRSp53 (unpublished data). The structural organization of the IMD-induced membrane tubules was examined in more detail by using electron tomography. Because of the complex nature of structures induced by 22 μM MIM/IMD-L (Fig. 1 D), 1.1 μM protein was used in this experiment. The tomography analysis of a selected section is displayed in Fig. 1 E and Video 1 (available at http://www.jcb.org/cgi/content/full/jcb.200609176/DC1). MIM/IMD-L–induced tubules were of regular width (measured diameter of 78 nm; SD = 7 nm; $n = 65$; the narrowest tubule

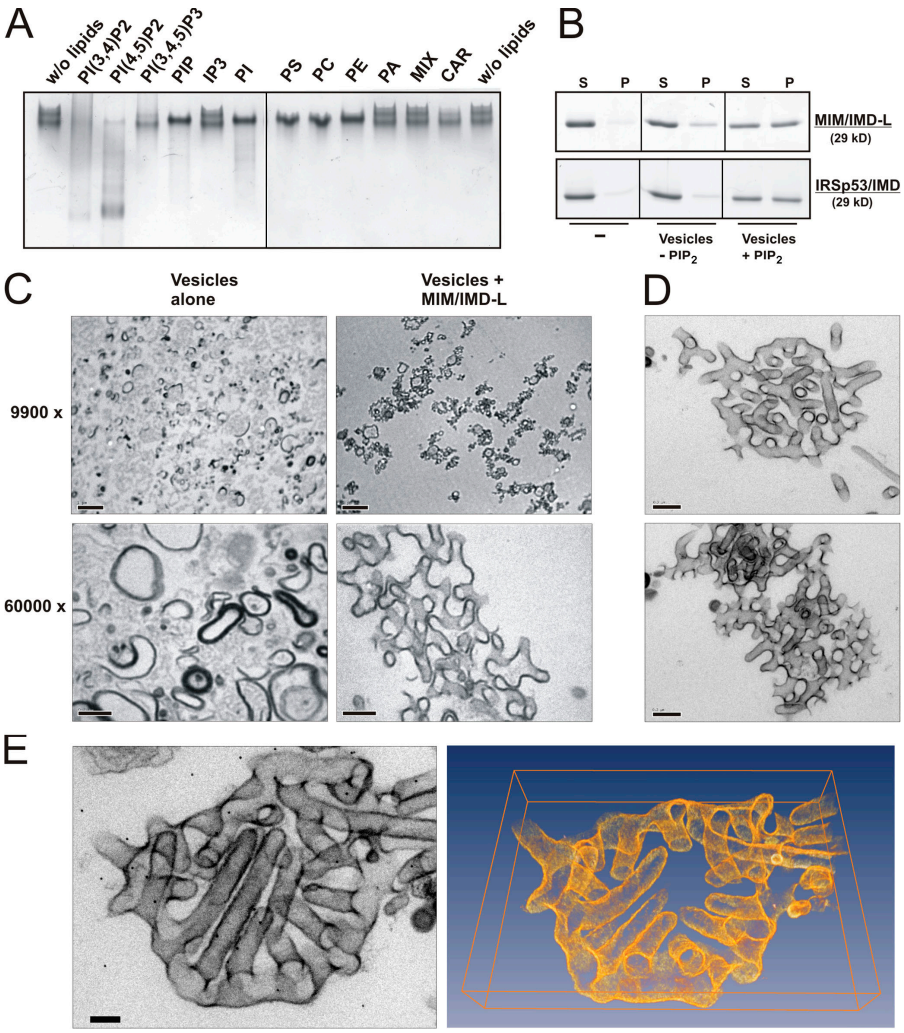

Figure 1. **IMDs bind and tubulate PI(4,5)P_2-rich membranes.** (A) Native gel electrophoresis analysis was performed with MIM/IMD-L alone (without lipids) or with MIM/IMD-L mixed with fivefold molar excess of different phospholipids. PI(3,4)P_2 and PI(4,5)P_2 caused MIM/IMD-L to move faster toward the anode, indicating an increase in negative charge and a binding interaction. IP_3, inositol(1,4,5) trisphosphate headgroup; PI, phosphatidylinositol; PA, phosphatidic acid; MIX, lipid mixture (cholesterol, lecithin, and lysolecithin); and CAR, cardiolipin. MIM/IMD-L without lipids was loaded to the first and last wells of the gels, respectively. (B) MIM/IMD-L and IRSp53/IMD cosedimented with PI(4,5)P_2-rich (30%) large multilamellar vesicles. More than 50% of MIM/IMD-L was found in the pellet fraction (P) in samples containing PI(4,5)P_2, whereas much weaker association is seen with vesicles without PI(4,5)P_2. (C) EM analysis of multilamellar vesicles containing 30% of PI(4,5)P_2 with and without MIM/IMD-L. Thin sections (60 nm) were visualized with transmission electron microscope. Images were taken with magnifications of 9,900 and 60,000. MIM/IMD-L clustered vesicles and deformed them into tubular network structures. Bars: (top) 1 µm; (bottom) 0.2 µm. (D) EM micrographs of 120-nm-thick sections of MIM/IMD-L deformed multilamellar (top) and unilamellar (bottom) vesicles containing 30% PI(4,5)P_2. Bars, 0.2 µm. (E) 3D electron tomography analysis of MIM/IMD-L induced tubular network. (left) EM micrograph of a 250-nm-thick section; (right) corresponding model where tubules that were not connected with the surface of the membrane within the reconstructed volume were removed. Membrane tubules (diameter of 78 nm) penetrate the vesicular structure. Bar, 0.1 µm.

was 60 nm and the widest 93 nm) independent of the protein concentration (unpublished data). Amount of tubulation corresponded with the amount of protein, and similar tubulation was observed in assays performed either with unilamellar or multilamellar vesicles (Fig. 1 D). In contrast to the long tubular extensions induced by BAR/F-BAR domains, electron tomography revealed that in intact vesicular structures MIM/IMD-induced tubules are typically invaginating toward the interior of the vesicle (Fig. 1 E and Video 1). This observation suggests that IMDs tubulate membranes in a direction opposite that of BAR/F-BAR domains. It is also important to note that the amount of membrane tubulation induced by MIM/IMD correlated with the PI(4,5)P_2 density of the vesicles. High amounts of membrane tubules were observed in experiments performed with 10–30% PI(4,5)P_2 density. MIM/IMD also induced membrane tubulation at 3–5% PI(4,5)P_2, but this was less efficient than higher PI(4,5)P_2 density (Fig. S1 C). Only very weak tubulation was detected with vesicles without PI(4,5)P_2 (unpublished data). We also performed a similar assay by using two other PI(4,5)P_2-binding proteins, α-actinin and heterodimeric capping protein. These proteins did not induce membrane tubulation under similar conditions, confirming that this activity is not a general feature of PI(4,5)P_2-bnding proteins (unpublished data).

Mapping of the actin and PI(4,5)P_2-binding sites of the IMD

To reveal the mechanisms of actin and phospholipid interactions of the IMD, the PI(4,5)P_2- and actin-binding sites of MIM/IMD-L were mapped by systematic mutagenesis. 19 clusters of mutations were individually created on the surface of MIM/IMD-L using the 3D structure of the domain (Lee et al., 2007) as a guide. Each cluster of mutations contained one to three charged amino acids or surface-exposed hydrophobic residues substituted with alanines. The mutant clusters are evenly distributed over the surface of the IMD (Fig. 2, B and C; and Fig. S3 A).

The PI(4,5)P_2 binding was examined by high-speed cosedimentation assay with synthetic lipid vesicles containing 30% PI(4,5)P_2. Eight mutants displayed a substantially reduced affinity for PI(4,5)P_2 (Fig. 2 A and Fig. S3 B). Five of these (Mut10, -11, -12, -15, and -16) were clusters of charged residues that map close to the distal ends of the dimeric IMD, and two (Mut14 and -17) contained substitutions of surface-exposed hydrophobic residues. These data show that the PI(4,5)P_2-binding site of IMD consists of relatively large positively charged regions that are located at each end of the dimeric domain. This is further supported by the observation that neutralizing the negative charge within this region (Mut13 [D143A]) increased the affinity

A

Mutants	Amino Acids	Effect on Actin Binding	Effect on PIP_2 binding
MIM/IMD-L		+++	+++
MIM/IMD-S		+++	++++
Mut 1	K7A	+++	+++
Mut 2	L15A	+++	+++
Mut 3	E31A	+++	+++
Mut 4	K60A, D63A	+++	+++
Mut 5	R69A, R73A	+++	+++
Mut 6	R73A, E74A	+++	++
Mut 7	R81A, R85A	+++	+++
Mut 8	R87A	+++	+++
Mut 9	E110A, E113A	+++	+++
Mut 10	K124A, D125A	+++	++
Mut 11	E129A, K131A, K132A	++	+
Mut 12	K138A, K139A	++	+
Mut 13	D143A	++++	++++
Mut 14	L145A, L147A	+++	+
Mut 15	K146A, K149A, K150A	++	+
Mut 16	K152A, K153A, R159A	++	+
Mut 17	L170A	+++	++
Mut 18	R189A, K190A	+++	+++
Mut 19	K239A	+++	+++
Mut 15+12	K146A, K149A, K150A, K138A, K139A	+	+/-
Mut 15+11	K146A, K149A, K150A, E129A, K131A, K132A	+	+/-
Mut 15+10	K146A, K149A, K150A, K124A, D125A	+	+/-
Mut 15+16	K146A, K149A, K150A, K152A, K153A, R159A	+	+/-
Mut 17+14	L170A, L145A, L147A	+++	++

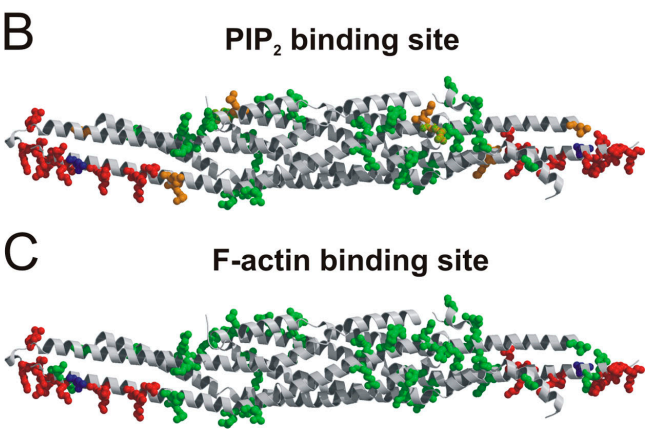

Figure 2. **Determination of PI(4,5)P_2- and F-actin–binding sites of the IMD.** (A) A list of mutants examined in this study. The PI(4,5)P_2- and F-actin–binding properties of the mutants were determined by cosedimentation assays. The data obtained from F-actin–binding assays performed with four actin concentrations and from three independent PI(4,5)P_2-binding assays are displayed (see Fig. S3, B and C, available at http://www.jcb.org/cgi/content/full/jcb.200609176/DC1, for the data). Affinities of mutant proteins as compared with wild-type IMD are indicated. (B) The residues mutated in this study are shown as ball and stick in the ribbon structure of MIM/IMD-L (Lee et al., 2007). Residues without detectable effects to PI(4,5)P_2 binding are in green. Residues with moderate and strong defects in binding are in orange and in red, respectively. Substitution of Asp 143 (blue) by Ala resulted in an increase in PI(4,5)P_2 binding. (C) Presentation of the F-actin–binding site of MIM/IMD-L with the same color coding.

of IMD for PI(4,5)P_2. In addition, surface-exposed leucines located in these regions contribute to PI(4,5)P_2 binding.

Actin filament cosedimentation assay performed with 1 μM IMD and 0–10 μM F-actin revealed that only four clusters of mutations (Mut11, -12, -15, and -16) displayed considerably lower affinity for F-actin as compared with wild-type IMD. Combining these mutations further reduced F-actin binding, demonstrating the importance of these residues for actin interactions (Fig. 2 A and Fig. S3 C). These residues map close to the ends of the dimeric IMD and overlap with the PI(4,5)P_2-binding site, revealing that the positively charged region located in helix-2 forms the main actin- and PI(4,5)P_2-binding site of the IMD (Fig. 2 C). As with the observed increase in PI(4,5)P_2 binding, neutralization of the negative charge within this region (Mut13 [D143A]) also increased the affinity of IMD to F-actin. However, in contrast to PI(4,5)P_2 binding, none of the mutants (or double mutants) resulted in a complete lack of F-actin binding, showing that IMDs interact with F-actin mostly through nonspecific electrostatic interactions. To confirm the integrity of the mutants, we performed a urea denaturation assay for each double mutant used in the study. The mutants unfolded at the same urea concentration (4.5 M) as wild-type MIM/IMD, indicating that the mutations did not affect folding of the protein (unpublished data).

PI(4,5)P_2 binding of MIM/IMD is required for filopodia formation

Expression of IMDs in cultured mammalian cells induces a dramatic formation of filopodia (Yamagishi et al., 2004; Gonzalez-Quevedo et al., 2005; Millard et al., 2005). However, the dynamics of these structures (i.e., whether they are true membrane protrusions or the result of cell retraction) have not been reported. Live-cell analysis of U2OS cells expressing MIM/IMD-L revealed that IMD-induced filopodia are highly dynamic and extend with a rate of up to 1 μm/min (Fig. 3 A and Video 2, available at http://www.jcb.org/cgi/content/full/jcb.200609176/DC1). These protrusions are dependent on an intact actin cytoskeleton because treatment of the cells with latrunculin A decreased the dynamics of IMD-induced filopodia (Video 3). Quantification of the data revealed that ~40% of the filopodia in untreated cells displayed elongation during the 60-s detection period, whereas after 6, 12, or 18 min of latrunculin A treatment, <5% of the filopodia displayed elongation.

To examine the in vivo roles of PI(4,5)P_2 interactions of IMD, we assayed filopodia formation in U2OS cells expressing mutant IMDs. One of these (Mut12+15) displays severe defects in F-actin binding and a nearly complete lack of PI(4,5)P_2 binding (Fig. 2) and loss of lipid vesicle tubulation activity (unpublished data). The other mutant (Mut14+17) interacts with F-actin with a similar affinity to wild-type IMD but shows a moderate defect in PI(4,5)P_2 binding (Fig. 2 A and Fig. S3, B and C). The mutant defective in actin and PI(4,5)P_2 binding failed to induce detectable filopodia in U2OS cells. Interestingly, Mut14+17, which displays defects only in PI(4,5)P_2 binding, induced significantly less filopodia than wild-type IMD (Fig. 3 B). This demonstrates that interaction with PI(4,5)P_2 is critical for filopodia formation by IMDs.

MIM/IMD localizes to the interface between F-actin bundles and plasma membrane

The experiments described above showed that IMDs bind and deform PI(4,5)P_2-rich membranes in vitro and that the PI(4,5)P_2

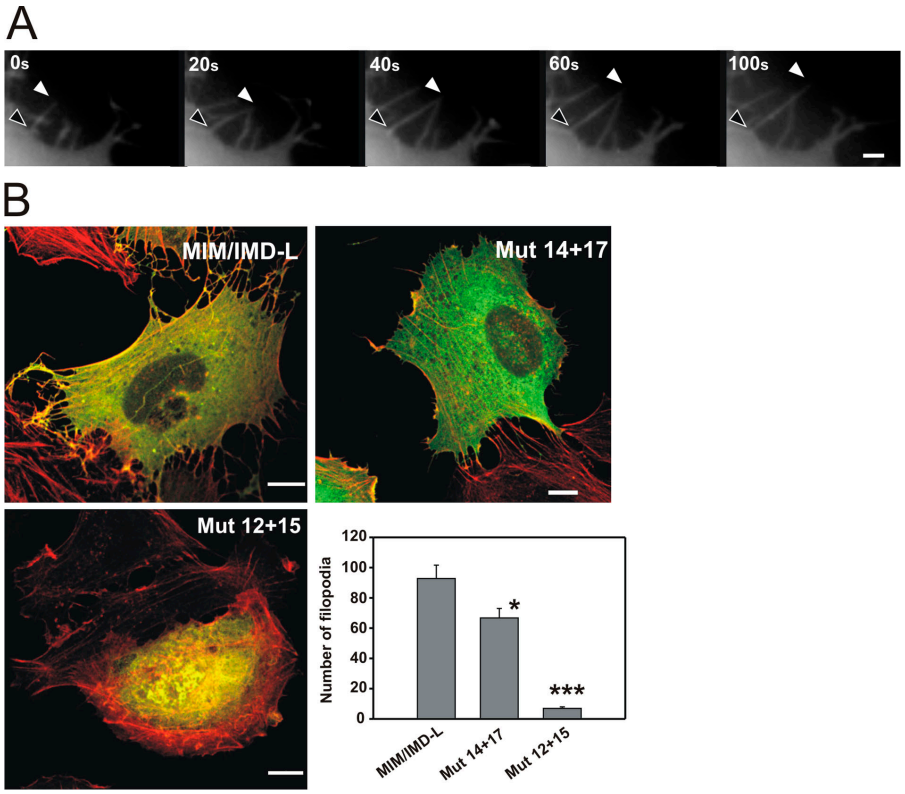

Figure 3. **Compromised lipid binding weakens the ability of an IMD to induce dynamic filopodia.** (A) Time-lapse images of a U2OS cell expressing GFP-tagged MIM/IMD-L. The black arrowhead shows the cell edge, and the white arrowhead indicates the tip of a growing filopodium. The filopodium extended with a rate of ~1 μm/min. Bar, 1 μm. (B) Confocal images from U2OS cells overexpressing GFP-tagged wild-type and mutant forms of MIM/IMD-L. Mut12+15, which has severe defects in both F-actin and PI(4,5)P_2 binding in vitro did not induce filopodia formation in cells. Mut14+17, which displayed moderate defects in PI(4,5)P_2 binding but bound F-actin with wild-type affinity in vitro, showed reduced filopodia formation compared with wild-type MIM/IMD-L. F-actin is in red. Bar, 10 μm. Quantification of the number of filopodia per cell is shown in the diagram. SEM values are indicated as error bars. Analysis (*t* test) of the number of filopodia shows results to be statistically significant ($n = 20$). ***, $P < 0.001$; *, $P < 0.05$.

binding appears critical for the filopodia-inducing activity in vivo. 3D analysis, derived from seven confocal planes of filopodia from cells expressing GFP-tagged MIM/IMD-L, revealed that the IMD does not localize to the F-actin bundle but instead localizes to the plasma membrane surrounding the F-actin bundle. The divergent localization was most obvious at the base of the filopodium, where the GFP–MIM/IMD-L signal followed the plasma membrane rather than the F-actin bundle that extended into the cytoplasm (Fig. 4 A, right). In Fig. 4, MIM/IMD that does not colocalize with F-actin is shown in green. Because it surrounds the interior of filopodia, the colocalization (yellow) and F-actin (red) signals are not visible in thin filopodia when all channels are merged. A more detailed analysis revealed that F-actin and MIM/IMD colocalized only at a thin region within the filopodia (Fig. 4 A, middle). The channel correlation in colocalized volume, taking into account all the pixels in the 3D projection, was 0.6713 (calculated by Pearson's correlation coefficient, where 1 represents perfect colocalization, 0 is no colocalization, and −1 is perfect inverse colocalization). Together, these data demonstrate that MIM/IMD does not localize to the F-actin bundle but is instead found at the plasma membrane surrounding the bundle. Colocalization channel analysis further confirmed only a very thin interface where both proteins are present.

To investigate the possible cooperation between lipid- and actin-binding activities of IMDs, we examined samples containing PI(4,5)P_2-rich vesicles, F-actin, and IMD by light microscopy. Alexa 568–labeled F-actin, MIM/IMD-L, and fluorescein phosphatidylethanolamine (PE)–labeled vesicles with or without PI(4,5)P_2 were mixed, applied on polyornithine-coated glass slides, and imaged by light microscopy. In the presence of MIM/IMD-L and PI(4,5)P_2, clear actin dots were found to localize at positions corresponding to vesicles (Fig. 4 B). Importantly, vesicles without PI(4,5)P_2 showed significantly weaker colocalization with actin, as was also found for PI(4,5)P_2 vesicles in an experiment using Mut15 (Fig. 4, B and C). The intensity of actin staining on vesicles was quantified, confirming the importance of PI(4,5)P_2 binding of IMD in the formation of these denser F-actin dots (Fig. 4 C). Similar results were also obtained with the IMD of IRSp53 (unpublished data). The results demonstrate that IMDs are capable of associating actin filaments with PI(4,5)P_2 vesicles, at least in vitro. However, it is important to note that the actin and PI(4,5)P_2-binding sites overlap on the surface of the IMD (Fig. 2). This suggests that a fraction of IMDs associates in this assay with membranes only through one pole, leaving the other binding site accessible to actin. Alternatively, the membrane-bound IMD may interact with actin through partially different interface than the soluble domain.

F-actin–bundling and Rac-binding activities of IMDs do not contribute to filopodia formation

IMDs were previously reported to induce filopodia formation through their actin filament–bundling activity (Yamagishi et al., 2004; Gonzalez-Quevedo et al., 2005; Millard et al., 2005). However, our data showed that IMDs bind and deform membranes and do not localize to actin bundles in filopodia, as would be expected for an F-actin cross-linking protein. We thus performed low-speed sedimentation assays to compare F-actin–bundling activities of IMDs. Surprisingly, at physiological ionic

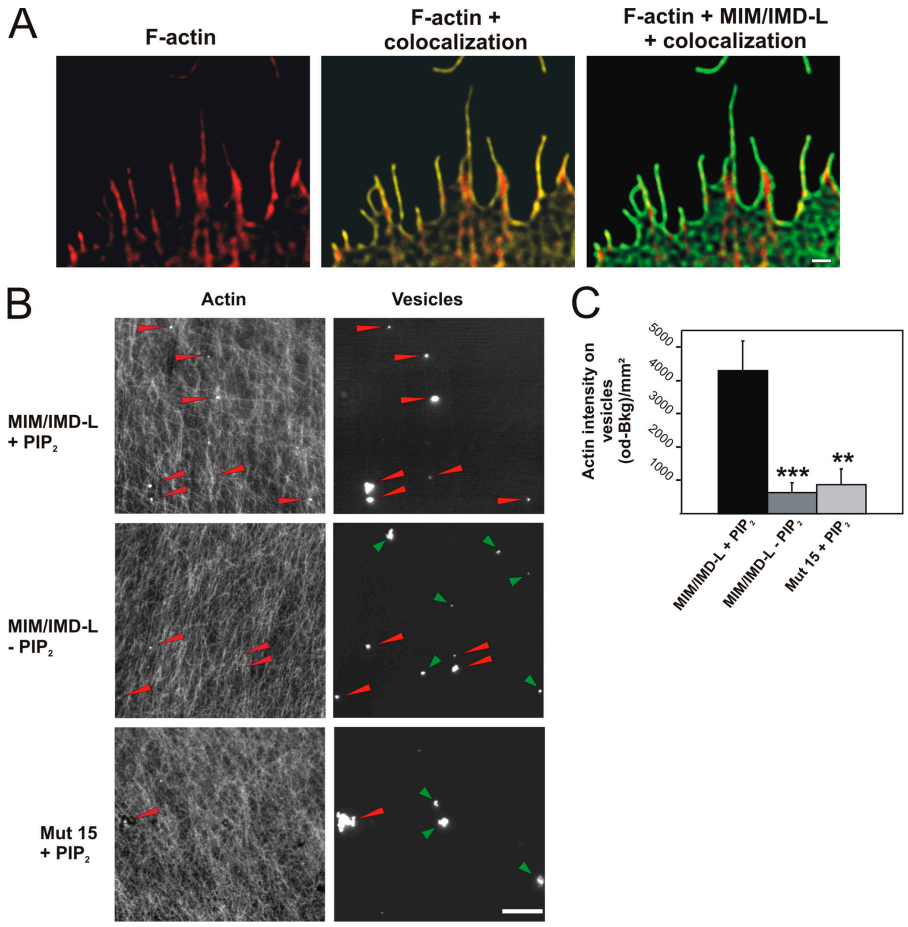

Figure 4. **MIM/IMD-L localizes to the plasma membrane in filopodia and associates actin to membranes in vitro.** (A) GFP–MIM/IMD-L localized to the plasma membrane and coated the F-actin bundles in filopodia of U2OS cell. 3D analysis derived from seven confocal planes shows F-actin in red (all panels), MIM/IMD in green (right), and colocalization in yellow (middle and right). Colocalization area (built by ImarisColoc software) is only a thin layer between actin and MIM/IMD and is almost invisible when the three channels are merged (right), as the MIM/IMD signal at the plasma membrane covers the interior of filopodia. Bar, 1 μm. (B) In vitro light microscopy assay. 1 μM F-actin (50% Alexa 568–labeled), 2.5 μM MIM/IMD-L, and 1.67 μM lipid vesicles (0/30% $PI[4,5]P_2$) were mixed and applied on polyornithine-coated glass slides for imaging. In the presence of MIM/IMD-L and $PI(4,5)P_2$, actin concentrated at the sites of vesicles, indicating MIM/IMD-L–associating actin and vesicles (top). MIM/IMD-L with vesicles without $PI(4,5)P_2$ or MIM/IMD-L Mut15, which displays defects in actin and $PI(4,5)P_2$ binding, induced much weaker colocalization between actin and vesicles. Red arrowheads indicate vesicles that show clear colocalization with actin, and green arrowheads indicate vesicles without colocalizing actin. Bar, 20 μm. (C) The intensity of the actin staining on the vesicles was quantified from 19–20 randomly selected vesicles. Error bars indicate SEM values. A *t* test was used to analyze p-values and showed statistically significant differences (***, $P < 0.001$; **, $P < 0.01$).

conditions, MIM/IMD-L, MIM/IMD-S, and IRSp53/IMD displayed almost undetectable F-actin–bundling activity (Fig. 5, A and C), even though these proteins bound F-actin with affinities similar to the one previously reported for IMDs (Fig. S3 C). Under identical conditions, 1.25 μM α-actinin efficiently bundled F-actin, suggesting that at physiological salt concentration, IMDs display only very weak actin filament–bundling activity (Fig. 5 A).

Because some previous F-actin bundling assays with IMDs were performed at low ionic strength (Millard et al., 2005) and IMDs appear to have a tendency to aggregate at low salt (Fig. 5 D), we performed a low-speed F-actin sedimentation assay at various salt concentrations. These data showed that the F-actin–bundling activity of IMDs (i.e., the amount of actin in the pellet fraction) increased sharply at low ionic strength (Fig. 5, B and C). We next used dynamic light scattering (DLS) to reveal whether the increased F-actin–bundling activity at subphysiological salt concentrations resulted from aggregation of MIM/IMD-L. DLS measures the fluctuation of scattered light, giving the distribution of hydrodynamic radii, $I(R_h)$. Thus, DLS not only provides the information about the size (hydrodynamic radius; R_h) but also about the polydispersity of the sample (Kainov et al., 2003). DLS performed at different KCl concentrations revealed a peak corresponding to the apparent size of IMD dimer and peaks of larger radius corresponding to protein aggregates. At 100 mM KCl, the amount of aggregates was small, keeping in mind that the intensity of the peaks is proportional to the square of molecular mass and thus strongly enhances the signal from large particles. At lower salt concentrations, the amount of particles with R_h of >50 nm increased dramatically, indicative of protein aggregation (Fig. 5 D). Similar results were also obtained from a high-speed sedimentation assay, which demonstrated that MIM/IMD-L precipitated at low salt (unpublished data). Together, these data suggest that the previously reported F-actin–bundling activity of IMDs resulted from protein aggregation at nonphysiological ionic conditions. IMDs display only very weak F-actin bundling at physiological conditions that is unlikely to contribute to filopodia formation in vivo. Furthermore, our analysis revealed that MIM/IMD-L does not bind G-actin or affect the nucleotide exchange or kinetics of actin polymerization (unpublished data).

We next compared the binding of MIM/IMD-L and -S to recombinant Rac by GST pull-down and surface plasmon resonance (SPR) assays. Surprisingly, these assays revealed a clear difference between MIM/IMD splice variant binding to Rac. In the GST pull-down assay, MIM/IMD-S interacted with dominant-active (V12) and -inactive (N17) Rac, as described previously (Bompard et al., 2005), whereas no detectable binding of MIM/IMD-L to Rac was seen in this assay (Fig. 6 A). In the SPR assay, a concentration-dependent interaction of MIM/IMD to Rac was studied. Consistent with the pull-down assays, the obtained equilibrium binding level values showed that Rac

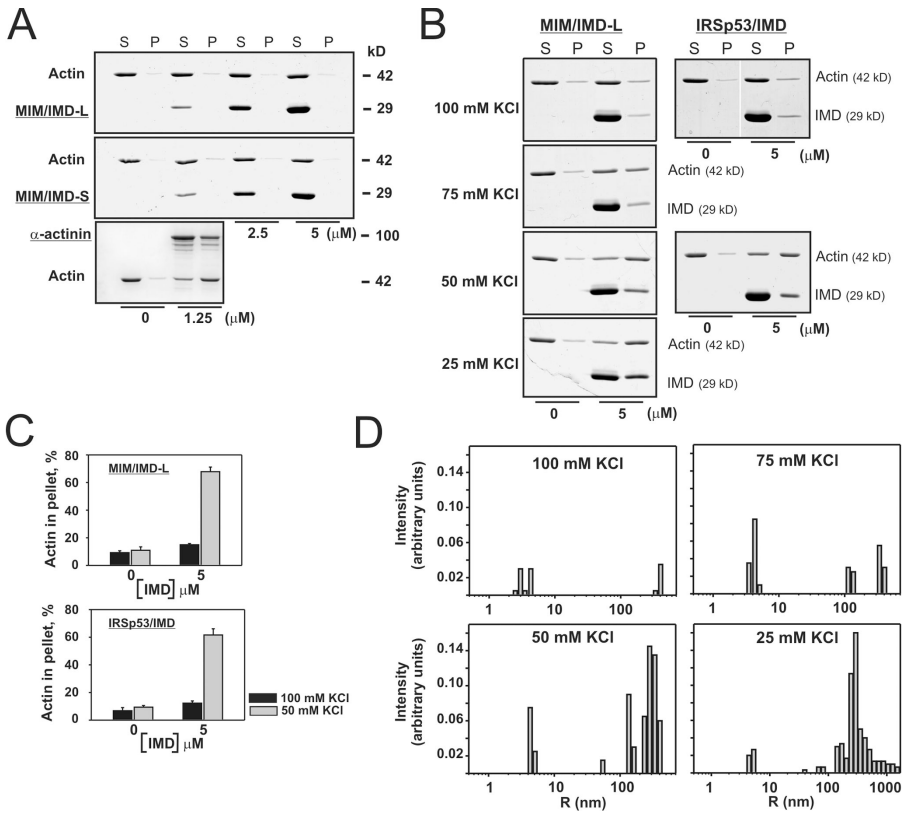

Figure 5. **IMDs display weak F-actin–bundling activity at physiological ionic strength.** (A) Low-speed F-actin sedimentation assay, where actin bundles sedimented into the pellet fraction (P), whereas unbundled F-actin stayed in the supernatant (S). F-actin concentration was 2 μM, and MIM/IMD dimer concentrations were 0, 1.25, 2.5, and 5 μM. Human α-actinin was used as a control in dimer concentration of 1.25 μM. Note that although α-actinin efficiently cross-linked F-actin, neither MIM/IMD-L or -S induced detectable F-actin bundling in this assay. (B) Low-speed F-actin sedimentation assay repeated in buffers containing different concentrations (100, 75, 50, or 25 mM) of KCl. The actin-bundling activity of both MIM/IMD-L and IRSp53/IMD increased at lower KCl concentrations. (C) Quantification of F-actin–bundling activities of IMDs from three independent experiments at 100/50 mM KCl. Error bars indicate standard deviations. (D) DLS profiles of MIM/IMD-L at 100, 75, 50, or 25 mM KCl. The amount of aggregates >50 nm in hydrodynamic radius increased at lower KCl concentrations. The mean of R_h distributions of two independent measurements is presented in the graphs.

interacted with MIM/IMD-L with a binding level of only 10–15% of that of MIM/IMD-S (Fig. 6 B). A high background was obtained from the His-GST control channel, which makes the observed affinity of the MIM/IMD-L variant difficult to interpret, further proposing a very weak Rac interaction for this variant. Furthermore, our pull-down and SPR assays demonstrated also that neither variant of MIM/IMD bound other small GTPases, such as RhoA and/or Cdc42, with detectable affinity (unpublished data).

Although only MIM/IMD-S binds Rac with detectable affinity, overexpression of either MIM/IMD-S or -L induced filopodia formation in cells (Fig. 6 C). Quantification of filopodia number from transfected cells revealed no apparent differences between cells expressing MIM/IMD-S and -L (Fig. 6 D). This provided evidence that, in contrast to $PI(4,5)P_2$ binding (Fig. 3 B), Rac binding is not necessary for filopodia formation by IMDs.

Discussion

IRSp53 and MIM are relatively large, multidomain proteins that regulate cytoskeletal dynamics during motile and morphogenetic processes. Expression of full-length proteins or their N-terminal IMDs, which bind Rho family GTPases and bundle actin filaments, results in dramatic filopodia/microspike formation in cultured mammalian cells (Yamagishi et al., 2004; Bompard et al., 2005). In this study, we determined the mechanism by which IMDs induce membrane protrusions in cells. We show that (1) IMDs display only very weak F-actin–bundling activity at physiological ionic conditions that is unlikely to contribute to filopodia formation. The previously reported actin-bundling activity appears to result from protein aggregation at low salt conditions. (2) Interaction with small GTPase Rac is not required for IMD-induced filopodia formation. (3) IMDs bind and deform $PI(4,5)P_2$-rich lipid membranes in vitro and localize to the interface of plasma membrane and F-actin bundles in filopodia. (4) IMDs interact with membranes through a similar interface to the structurally related BAR domains. However, IMDs and BAR domains generate an opposite membrane curvature because of the different geometries of their membrane-binding interfaces. (5) Interaction with $PI(4,5)P_2$-rich membranes is necessary for the filopodia-inducing activity of IMDs. Together, these findings show that IMD is a new functional member of the membrane-deforming BAR domain family. However, in contrast to previously characterized membrane-deforming domains, IMDs induce formation of membrane protrusions rather than invaginations.

Here, we show that, in contrast to previous studies (Yamagishi et al., 2004; Gonzalez-Quevedo et al., 2005; Millard et al., 2005), the IMD does not function as an F-actin–bundling motif at physiological ionic conditions. Although the IMD does not bundle F-actin, it binds actin filaments with a moderate affinity. Previous charge-reversal mutagenesis studies revealed that a cluster of four positively charged residues at the ends of IMD dimer plays a central role in F-actin binding and bundling (Bompard et al., 2005; Millard et al., 2005). Our systematic mutagenesis analysis revealed that the F-actin–binding site of the IMD of MIM is considerably larger and covers an ∼4-nm-long positively charged region along helix-2. Importantly, none of the mutations in this study resulted in a complete lack of F-actin binding.

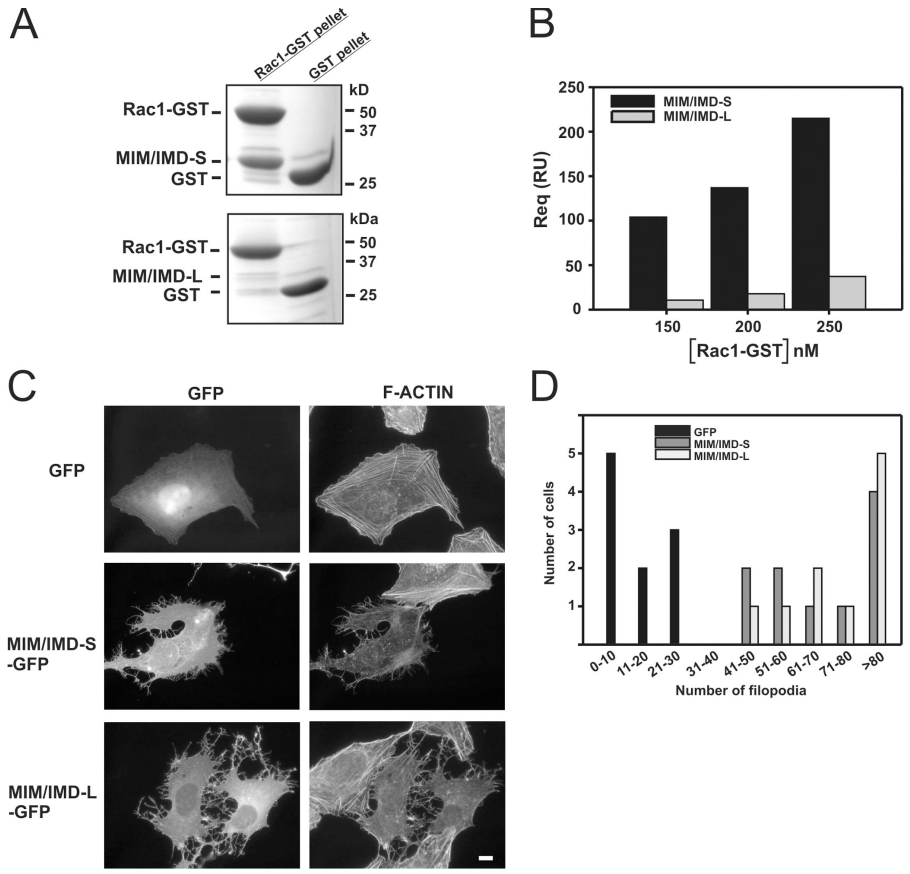

Figure 6. **Interaction with small GTPase Rac is not required for IMD-induced filopodia formation.** (A) The binding of MIM/IMD variants to Rac was determined by a GST pull-down assay under physiological ionic conditions. GST fusion of recombinant Rac (V12) or GST alone were coupled to glutathione–Sepharose beads and incubated with MIM/IMD splice variants. The beads were sedimented, washed three times, and loaded on SDS gels. MIM/IMD-S clearly bound Rac, whereas no binding of MIM/IMD-L was detected with this assay. (B) The binding of GST-Rac (V12) to MIM/IMD variants examined with a Biacore 2000. The histograms represent the equilibrium binding levels (Req) in resonance units that were obtained for each Rac concentration with binding of MIM/IMD-L or -S. (C) U2OS cells overexpressing GFP-tagged MIM/IMD-S or -L. Both MIM/IMD variants induced filopodia-like protrusions in cells in a similar manner. F-actin visualized with Alexa 568 phalloidin. Bar, 10 μm. (D) Quantification of filopodia number in GFP, GFP–MIM/IMD-L, and GFP–MIM/IMD-S transfected U2OS cells (n = 10). Between MIM/IMD splice variants no difference was seen, suggesting that Rac binding is not required for this activity.

Even mutants in which five lysines/arginines were replaced by alanines bound F-actin with detectable affinity. This suggests that IMDs do not display a specific actin-binding site, but instead interact with F-actin through unspecific electrostatic interactions. In contrast, neutralizing specific residues at the actin-binding sites of other proteins such as actin-depolymerizing factor/cofilin or capping protein results in dramatic defects in actin binding (Lappalainen et al., 1997; Wear et al., 2003). The affinity of IMDs to F-actin is relatively low compared with most other F-actin–binding proteins (Yamagishi et al., 2004; Millard et al., 2005), suggesting a nonspecific interaction with actin. In filopodia, the IMD of MIM did not localize to F-actin bundles, as would be expected for an actin-bundling protein. At physiological ionic strength, this domain displayed an extremely weak actin-bundling activity compared with the well-characterized cross-linking protein, α-actinin (Fig. 5). Efficient bundling was, on the other hand, induced by subphysiological ionic conditions, where IMDs also form aggregates. It is important to note that although the IMD dimer contains two F-actin–binding sites, usually indicative of cross-linking activity, it appears to bind F-actin with relatively low affinity. Therefore, simultaneous interaction of both sites with F-actin, required to induce filament cross-linking, is likely to be a rare event. Alternatively, the actin filament may interact with these sites in an orientation that sterically prevents the binding of another filament. Together, these data suggest that IMDs do not bundle F-actin in cells.

MIM binds and activates Rac through its IMD. The Rac-binding site is located at the ends of the IMD dimer and overlaps with the actin-binding site (Bompard et al., 2005). Here, we show that only the shorter splice variant of MIM's IMD interacted with Rac, whereas the longer splice variant containing a four-amino-acid insertion in the loop between helix-2 and -3 did not bind Rac or other Rho-family GTPases with a detectable affinity. In the 3D structure, the insertion in MIM/IMD-L is located at the ends of IMD dimer, providing further support that this region plays a central role in Rac binding. Importantly, both MIM/IMD-L and -S, which displayed dramatic differences in Rac binding, induced similar filopodia formation when expressed in cells. These data, together with previous studies showing that filopodia formation by IMDs was not perturbed by the coexpression of dominant-negative Cdc42 or Rac1 (Yamagishi et al., 2004), provided evidence that Rac binding is not a critical function of IMDs during the formation of membrane protrusions. However, the differences between the two MIM splice variants in Rac binding suggest another, more specific role for this interaction in the context of the full-length proteins.

Our biochemical and EM analyses revealed that IMDs bind phosphatidylinositides and deform membranes into tubular structures. The observed $PI(4,5)P_2$ binding is in line with recent data showing that the N-terminal region of IRSp53 (containing the IMD) binds phospholipids in vitro (Suetsugu et al., 2006a). IMDs did not bind IP_3, the polar headgroup of $PI(4,5)P_2$, with detectable affinity. This result also implicates that the fatty acid chains of $PI(4,5)P_2$ are important for the interaction or that IMD interacts only with membranes where the

inositol headgroups are aligned. The latter alternative is supported by our mutagenesis analysis, revealing that the PI(4,5)P_2-binding site is composed of relatively large positively charged surfaces at each end of the dimer. Although the peculiar symmetry of IMDs results in an ~140° rotation of the dimer ends to each other, the two positively charged PI(4,5)P_2-binding patches are facing the same direction when the domain is aligned with amphiphysin BAR domain (Fig. 7 A). This model shows that IMDs bind lipids through an interface similar to that found in BAR domains. It is also important to note that membrane, Rac, and actin binding seem to take place roughly through the same area of the molecule, suggesting that these interactions compete with each other. However, of these activities, only PI(4,5)P_2 binding is necessary for the filopodia formation, suggesting that the other (competitive) interactions may have a regulatory role.

The membrane-tubulation activity of IMDs is also supported by a recent study, which demonstrated that the IMD of IRSp53 can deform PI(3,4,5)P_3-rich membranes in vitro (Suetsugu et al., 2006b). However, this activity was reported to be Rac dependent, whereas our data demonstrates that IMD-induced membrane tubulation is independent from Rac both in vitro and in vivo. Furthermore, in contrast to our study, the IMD of MIM was not capable in deforming membranes in the study by Suetsugu et al. (2006b). These differences may arise from the fact that these authors used PI(3,4,5)P_3 in their EM studies, whereas PI(4,5)P_2 was used in our study. Our results showed that MIM/IMD binds PI(4,5)P_2 with substantially higher affinity than PI(3,4,5)P_3 both at native gel electrophoresis and cosedimentation assays. Because PI(4,5)P_2 is also >25-fold more abundant at the plasma membrane than PI(3,4,5)P_3 (Rameh and Cantley, 1999), PI(4,5)P_2 is most likely the physiological binding partner of IMDs during membrane deformation/filopodia formation in cells. It is also important to note that the membrane-binding interface of an IMD determined in our work is much more extensive than the one identified by Suetsugu et al. (2006b). This may arise either from the different lipids used in these assays or from the more extensive mutagenesis approach that was applied in our study.

Importantly, several lines of evidence suggest that IMDs generate a membrane curvature opposite to that of BAR domains. (1) Our electron tomography analysis revealed that the tubular structures induced by MIM/IMD-L often penetrate toward the interior of the vesicular structure. In contrast, BAR and F-BAR domains deform liposomes into morphologically different, separate narrow tubes (Takei et al., 1999; Itoh et al., 2005; Tsujita et al., 2006). (2) The lipid-binding interfaces of BAR and IMDs display opposite curvatures (Fig. 7 A). Interestingly, the curvature of the PI(4,5)P_2-binding interface measured from a space-filling model of the 18-nm-long IMD dimer suggests that MIM/IMD would induce a formation of a membrane tubule with a diameter of ~95 nm. This corresponds well with the diameter of MIM/IMD-L–induced membrane tubules measured from electron micrographs (~80 nm). (3) When expressed in cells, IMDs induce filopodia, as compared with plasma membrane invaginations induced by BAR domains. Thus, in contrast to the previously characterized lipid-deforming domains (BAR, F-BAR, and ENTH/ANTH), IMDs appear to generate an opposite

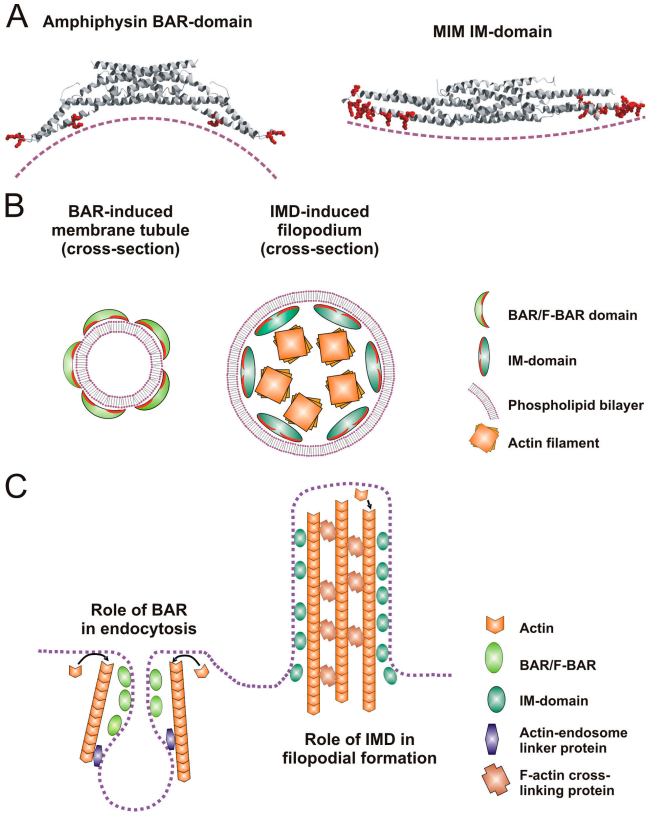

Figure 7. **Schematic model for the mechanism of filopodia formation by IMDs.** (A) Structures of amphiphysin BAR domain (left; Protein Data Bank ID: 1URU) and MIM/IMD (right; Protein Data Bank ID: 2D1L). The residues indicated in membrane binding in amphiphysin BAR (Itoh and De Camilli, 2006) and MIM/IMD (this study) are indicated in red. Purple dashed line indicates the proposed membrane interface. (B) Schematic model of membrane tubulation by BAR domain (left) and IMD (right). BAR domains form a coat outside of membrane tubule, whereas MIM/IMD curves the membrane in reversed orientation by binding to the inside of the tubule. (C) A side view of a BAR domain–induced endocytic invagination and an IMD-induced filopodium. Note that in addition to membrane-tubulating activities mediated by BAR and IMDs, both processes are also linked to actin dynamics.

membrane curvature. A hypothetical model for how IMDs induce filopodia formation through their membrane-tubulating activity is presented in Fig. 7 (B and C). In addition to membrane deformation, IMDs may also cross-link F-actin to the plasma membrane. However, further studies are required to elucidate the possible biological significance of this activity.

Actin dynamics are closely linked to membrane-deformation processes such as endocytosis (Kaksonen et al., 2006). Our data provide first evidence that, in addition to N-WASP–induced endocytic processes (Innocenti et al., 2005), plasma membrane protrusions are generated through interplay between actin polymerization machinery and direct membrane deformation. IRSp53 has been implicated in lamellipodia formation via WAVE/SCAR-2 complex and shown to activate WAVE2, an Arp2/3 activator (Miki et al., 2000; Choi et al., 2005; Suetsugu et al., 2006a). Localization of IRSp53 to the plasma membrane is dependent on its N-terminal IMD (Miki et al., 2000; Nakagawa et al., 2003; Choi et al., 2005; Suetsugu et al., 2006a). MIM localizes to filopodia, lamellipodia, and cell–cell junctions

(unpublished data), suggesting a role in actin-dependent morphogenetic processes at the plasma membrane. Similarly, several BAR domain proteins also interact with the regulators of actin dynamics. For example, yeast Rvs167/161 complex is intimately involved in actin assembly during endocytosis and mammalian tuba binds Arp2/3 activator N-WASP (Salazar et al., 2003; Kaksonen et al., 2005). Similarly, F-BAR proteins toca-1 and syndapin interact with N-WASP (Qualmann et al., 1999; Ho et al., 2004).

In conclusion, our study places the IMD in a new functional subbranch of the membrane-deforming BAR domain family. However, because of the unique geometry of its PI(4,5)P_2-binding site, an IMD induces membrane protrusions rather than invaginations. In the future, it will be important to reveal the detailed mechanism by which IMDs interact with membranes. Because IMDs have a tendency to form multimers at low salt conditions, it will be interesting to determine the possible role of the IMD oligomerization or cooperativity during membrane deformation. Elucidating the mechanism by which the interplay between different functions of IRSp53 and MIM (membrane deformation, actin monomer binding, and WAVE2 interactions) contribute to cell migration and morphogenesis will also provide important challenges for future research.

Materials and methods

Protein expression and purification

MIM/IMD-L was cloned into the SpeI–HindIII sites of pHAT1 vector (Peranen et al., 1996). The site-directed mutagenesis was performed as in Mattila et al. (2004). GFP fusions of MIM/IMDs were constructed into the XhoI–BamHI sites of pEGFP-N1 (CLONTECH Laboratories, Inc.). Alleles encoding mutant GTPases were cloned into BamHI–HindIII (Rac) or EcoRI–HindIII (RhoA, Cdc42) sites of pGEX-2T (GE Healthcare; Vartiainen et al., 2000). The human IRSp53 construct was provided by H. Nakagawa (Kyushu Institute of Technology, Kyushu, Japan), and IRSp53/IMD cDNA was cloned into SpeI–NsiI sites of pHAT1. All IMD constructs were expressed as His tag fusion proteins, enriched with Ni-NTA Superflow beads (Sigma-Aldrich), and purified with Q-Sepharose high-performance anion-exchange column (GE Healthcare). Small GTPases Rac, RhoA, and Cdc42 were expressed as GST fusion proteins, enriched with glutathione-agarose beads (Sigma-Aldrich), and purified by Superdex-75 HiLoad gel filtration column (GE Healthcare). Human skeletal muscle α-actinin 2 (provided by J. Ylänne, University of Jyväskylä, Finland) was expressed and purified from pET8c-6HTEV plasmid (Young and Gautel, 2000). Rabbit muscle actin was prepared from acetone powder as described by Pardee and Spudich (1982).

Preparation of lipid vesicles

PI(4,5)P_2 (L-α-phosphatidylinositol-4,5-bisphosphate; porcine brain triammonium salt), PI(3,4,5)P_3 (1,2-dioctanoyl-*sn*-glycero-3-[phosphoinositol-3,4,5-trisphosphate], tetra-ammonium salt), phosphatidylcholine (PC; brain), phosphatidylserine (PS; brain), and fluorescein PE (18:1 PE/CF 1,2-dioleoyl-*sn*-glycero-3-phosphoethanolamine-N-[carboxyfluorescein]) were purchased from Avanti Polar Lipids, Inc. PC and PS were dissolved in 9:1 chloroform/methanol, PI(4,5)P_2 was dissolved in 1:2 chloroform/methanol, PI(3,4,5)P_3 was dissolved in 65:35:8 chloroform/methanol/water, and fluorescein PE was supplied in chloroform. The following mixtures were prepared: 5% fluorescein PE, 20% PS, 45–75% PC, and 0–30% PI(4,5)P_2. Samples were vacuum dried under N_2 and hydrated for a minimum of 4 h in 0.2 mM Hepes-KOH, pH 7.5, and 100 mM NaCl to a total lipid concentration of 1 mM. Finally, the vesicles were vortexed thoroughly for 2 min to allow formation of large multilamellar vesicles. Vortexing was repeated before each experiment. When preparing unilamellar vesicles, hydrated lipids were subjected to extrusion through a 1-μm filter according to manufacturer's instructions (Mini-Extruder; Avanti Polar Lipids, Inc.).

EM

Vesicles (167 μM total lipid and 3, 5, or 30% PI[4,5]P_2) were mixed with 0, 1.1 (for tomography), or 22 μM IMD dimer in F-buffer (5 mM Tris-HCl, pH 7.5, 0.2 mM ATP, 0.2 mM DTT, 0.2 mM $CaCl_2$, 2 mM $MgCl_2$, and 100 mM KCl). Reactions were incubated for 30 min and fixed by adding 2.1% glutaraldehyde and 0.1 M Hepes for 30 min at RT. Samples were sedimented (17,000 *g* at 4°C) and postfixed by osmication (1% OsO_4, 15 mg/ml K_4[Fe{CN}$_6$], and 0.1 M Na-cacodylate buffer, pH 7.4), for 1 h, followed by en bloc staining with uranyl acetate (1% uranyl acetate and 0.3 M sucrose) for 1 h at 4°C, dehydration, and Epon embedding. Thin (60 nm) or semi-thick (120 nm) sections were prepared and stained with uranyl acetate and lead citrate for visualization with a transmission electron microscope (FEI Tecnai 12; FEI Corp.) operated at 120 kV. Images were recorded using a charge-coupled device camera (Erlangshen ES500W; Gatan Corp.).

Electron tomography

For 3D electron tomography, a 250-nm-thick section was prepared as described above and imaged with an electron microscope (Tecnai 20 FEG; FEI Corp.) operating at 200 kV. Images were recorded with a 1k × 1k charge-coupled device camera (Multiscan 794; Gatan Corp.) at a magnification of 11,500× (1.63 nm/pixel). For collection of tilt series, the specimen was tilted ±70° at 1° intervals around two orthogonal axes (Mastronarde, 1997). The alignment and reconstruction of tilt series was done with the IMOD program package (Kremer et al., 1996) using 10-nm colloidal gold particles as fiducial markers. The tomographic reconstruction was visualized and modeled with Amira software using volume rendering (TGS, Inc.).

Cosedimentation assays

Actin filament cosedimentation assays were performed as described previously (Mattila et al., 2003; Woodings et al., 2003). For lipid-binding assays, 20 μl of buffer (20 mM Hepes-KOH, pH 7.5, and 100 mM NaCl) or buffer with vesicles of 167 μM total lipid concentration was added to 25 μl of F-buffer. IMD constructs (5 μl) were diluted in desired concentrations in F-buffer. In high-speed (F-actin or vesicle binding) assays, samples were sedimented by centrifugation at 360,000 *g* for 30 min at RT. In low-speed F-actin bundling assays, samples were sedimented at 17,000 *g* for 30 min at 4°C. 12% SDS-polyacrylamide gels were scanned with a calibrated imaging densitometer (GS-710; Bio-Rad Laboratories, Inc.) and quantified with Quantity One software.

Cell culture and light microscopic methods

Immunofluorescence and transfection of human osteosarcoma (U2OS) cells with GFP-MIM/IMD constructs were performed as described by Hotulainen and Lappalainen (2006). F-actin was visualized with Alexa 568 phalloidin (dilution 1:400; Invitrogen). To block actin polymerization, cells were treated with 0.2 μg/ml latrunculin A (Invitrogen). For analysis of the association of actin and vesicles in vitro, samples containing 2.5 μM MIM/IMD-L dimer, 1.67 μM lipid vesicles (0 or 30% PI[4,5]P_2), and 1 μM F-actin (50% Alexa Fluor 568–labeled actin) were prepared for light microscopy in modified F-buffer (10 mM imidazole, pH 7.5, 0.2 mM $CaCl_2$, 0.2 mM ATP, 1 mM DTT, 100 mM KCl, 2 mM $MgCl_2$, and 1 mM EGTA). 2-μl samples from reactions were applied on polyornithine-coated glass slides. Images were acquired through a charge-coupled device camera (DP70; Olympus) on a microscope (AX70 Provis; Olympus). For the image acquirement, the AnalySIS software (Olympus) and PlanApo 60×/1.40 (oil) objective (Olympus) was used. For in vitro samples, images were acquired with fixed exposure times for quantification with TINA software. The confocal image stacks were deconvoluted with AutoQuant AutoDeblur 3D Blind Deconvolution (AutoQuant Imaging, Inc.), and the 3D reconstructions and the colocalization analysis were made with Bitplane Imaris (Bitplane Inc.). The time-lapse images were acquired with an inverted microscope (IX70; Olympus) equipped with a Polychrome IV monochromator (TILL Photonics) with the appropriate filters, heated sample environment, CO_2 control, and 40×/1.35 (oil) objective. Total internal reflectance fluorescence (TIRF) was performed using 60×/1.45 (oil) TIRF objective and 488 nm laser.

DLS

Samples (0.5 mg/ml of IMD in F-buffer with desired KCl concentrations) were prepared, incubated for 1 h at 20°C, and monitored with a batch DLS instrument (Precision Detectors) equipped with deconvolution software for correlation function analysis (Kainov et al., 2003).

GST pull-down assay

GST pull-down assays were performed as in Mattila et al. (2004). Beads containing 5 μM GST or GST-Rac (V12 and N17) were incubated with

2.5 μM MIM/IMD dimer in 10 mM Tris, pH 7.5, and 100 mM NaCl for 10 min at RT, washed three times with 500 μl of reaction buffer, and analyzed on 12% SDS-PAGE.

SPR measurement

Interaction of Rac with MIM/IMD was studied with SPR on nitrilotriacetic acid sensor chip on a Biacore 2000 (Biacore AB) with a flow rate of 20 μl/min according to the manufacturer's instructions. The assay was performed in 10 mM Hepes-KOH, pH 7.2, and 150 mM NaCl with an injection contact time of 5 min and a dissociation time of 10 min. The recombinant His-tagged MIM/IMD splice variants and His-tagged GST proteins were immobilized by nickel chelation on nitrilotriacetic acid sensor surface to saturating levels (in the range of 9,000 resonance units) to facilitate detection of putatively low-affinity interactions. Binding of GST-Rac to MIM/IMD splice variants was studied under the system conditions between 20 and 300 nM Rac concentrations. To obtain binding levels at steady state, the control sensorgram, coated with His-GST, was subtracted from each MIM/IMD sensorgram. The steady-state binding levels of sensorgrams were evaluated by Langmuir 1:1 binding model modified to mass transfer effect in Biacore Evaluation Software 3.1. The obtained equilibrium binding level responses are given as resonance units.

Miscellaneous

The coordinates for 3D structure of the MIM/IMD (Lee et al., 2007) were obtained from R. Dominguez (University of Pennsylvania, Philadelphia, PA). Protein concentrations were determined with a diode array spectrophotometer (8452A; Hewlett Packard) by using the calculated extinction coefficients for mouse MIM/IMD-L and -S (ε_{280} = 15,220 $M^{-1}cm^{-1}$), IRSp53/IMD (ε_{280} = 19,770 $M^{-1}cm^{-1}$), and actin ($\varepsilon_{290\text{-}340}$ = 26,600 $M^{-1}cm^{-1}$). The native PAGE analysis for detecting the lipid interaction of MIM/IMD was performed as previously described (Palmgren et al., 2001). Fluorescence-monitored urea denaturation assays were performed as described by Lappalainen et al. (1997).

Online supplemental material

Fig. S1 shows that MIM/IMD prefers $PI(4,5)P_2$ over $PI(3,4,5)P_3$, the binding affinity correlates with phosphoinositide density of vesicles, and MIM/IMD is capable of tubulating membranes with low $PI(4,5)P_2$ density. Fig. S2 illustrates two alternative splice variants of MIM/IMD. Fig. S3 shows the $PI(4,5)P_2$ and F-actin–binding experiments on MIM/IMD-L mutants. Video 1 shows electron tomography of MIM/IMD-induced membrane tubules. In Video 2, the dynamics of MIM/IMD-induced filopodia are shown, and Video 3 demonstrates that the dynamics of MIM/IMD-induced filopodia is abolished by latrunculin A treatment. Online supplemental material is available at http://www.jcb.org/cgi/content/full/jcb.200609176/DC1.

We thank Elina Ikonen and Mirkka Koivusalo for advice on the preparation of lipid vesicles and Roman Tuma for expertise on DLS. Petri Auvinen, Mikko Frilander, Elina Ikonen, Keith Kozminski, and Johan Peränen are acknowledged for critical reading of the manuscript. We thank Roberto Dominguez for discussions, comments on the manuscript, and providing MIM/IMD coordinates. Miia Bovellan, Ulla Holopainen, and Pirta Hotulainen are acknowledged for technical assistance, instructions with gel scanning and quantification, and expertise with microscopes, respectively. Hiroyuki Nakagawa and Jari Ylänne are acknowledged for providing the human IRSp53 and α-actinin 2 constructs.

This study was supported by grants from the Finnish Cancer Foundation and the Academy of Finland (grant 111865; to P. Lappalainen). P. Mattila was supported by fellowships from Viikki Graduate School in Biosciences, the Alfred Kordelin foundation, and the Research and Science Foundation of Farmos.

Submitted: 28 September 2006
Accepted: 9 February 2007

References

Bompard, G., S.J. Sharp, G. Freiss, and L.M. Machesky. 2005. Involvement of Rac in actin cytoskeleton rearrangements induced by MIM-B. *J. Cell Sci.* 118:5393–5403.

Callahan, C.A., T. Ofstad, L. Horng, J.K. Wang, H.H. Zhen, P.A. Coulombe, and A.E. Oro. 2004. MIM/BEG4, a Sonic hedgehog-responsive gene that potentiates Gli-dependent transcription. *Genes Dev.* 18:2724–2729.

Choi, J., J. Ko, B. Racz, A. Burette, J.R. Lee, S. Kim, M. Na, H.W. Lee, K. Kim, R.J. Weinberg, and E. Kim. 2005. Regulation of dendritic spine morphogenesis by insulin receptor substrate 53, a downstream effector of Rac1 and Cdc42 small GTPases. *J. Neurosci.* 25:869–879.

Gallop, J.L., C.C. Jao, H.M. Kent, P.J. Butler, P.R. Evans, R. Langen, and H.T. McMahon. 2006. Mechanism of endophilin N-BAR domain-mediated membrane curvature. *EMBO J.* 25:2898–2910.

Gonzalez-Quevedo, R., M. Shoffer, L. Horng, and A.E. Oro. 2005. Receptor tyrosine phosphatase-dependent cytoskeletal remodeling by the hedgehog-responsive gene MIM/BEG4. *J. Cell Biol.* 168:453–463.

Ho, H.Y., R. Rohatgi, A.M. Lebensohn, M. Le, J. Li, S.P. Gygi, and M.W. Kirschner. 2004. Toca-1 mediates Cdc42-dependent actin nucleation by activating the N-WASP-WIP complex. *Cell.* 118:203–216.

Hotulainen, P., and P. Lappalainen. 2006. Stress fibers are generated by two distinct actin assembly mechanisms in motile cells. *J. Cell Biol.* 173:383–394.

Innocenti, M., S. Gerboth, K. Rottner, F.P. Lai, M. Hertzog, T.E. Stradal, E. Frittoli, D. Didry, S. Polo, A. Disanza, et al. 2005. Abi1 regulates the activity of N-WASP and WAVE in distinct actin-based processes. *Nat. Cell Biol.* 7:969–976.

Itoh, T., and P. De Camilli. 2006. BAR, F-BAR (EFC) and ENTH/ANTH domains in the regulation of membrane-cytosol interfaces and membrane curvature. *Biochim. Biophys. Acta.* 1761:897–912.

Itoh, T., K.S. Erdmann, A. Roux, B. Habermann, H. Werner, and P. De Camilli. 2005. Dynamin and the actin cytoskeleton cooperatively regulate plasma membrane invagination by BAR and F-BAR proteins. *Dev. Cell.* 9:791–804.

Kainov, D.E., S.J. Butcher, D.H. Bamford, and R. Tuma. 2003. Conserved intermediates on the assembly pathway of double-stranded RNA bacteriophages. *J. Mol. Biol.* 328:791–804.

Kaksonen, M., C.P. Toret, and D.G. Drubin. 2005. A modular design for the clathrin- and actin-mediated endocytosis machinery. *Cell.* 123:305–320.

Kaksonen, M., C.P. Toret, and D.G. Drubin. 2006. Harnessing actin dynamics for clathrin-mediated endocytosis. *Nat. Rev. Mol. Cell Biol.* 7:404–414.

Kremer, J.R., D.N. Mastronarde, and J.R. McIntosh. 1996. Computer visualization of three-dimensional image data using IMOD. *J. Struct. Biol.* 116:71–76.

Krugmann, S., I. Jordens, K. Gevaert, M. Driessens, J. Vandekerckhove, and A. Hall. 2001. Cdc42 induces filopodia by promoting the formation of an IRSp53:Mena complex. *Curr. Biol.* 11:1645–1655.

Lappalainen, P., E.V. Fedorov, A.A. Fedorov, S.C. Almo, and D.G. Drubin. 1997. Essential functions and actin-binding surfaces of yeast cofilin revealed by systematic mutagenesis. *EMBO J.* 16:5520–5530.

Lee, S.H., F. Kerff, D. Chereau, F. Ferron, A. Klug, and R. Dominguez. 2007. Structural basis for actin-binding function of missing-in-metastasis. *Structure.* 15:145–155.

Lee, Y.G., J.A. Macoska, S. Korenchuk, and K.J. Pienta. 2002. MIM, a potential metastasis suppressor gene in bladder cancer. *Neoplasia.* 4:291–294.

Lin, J., J. Liu, Y. Wang, J. Zhu, K. Zhou, N. Smith, and X. Zhan. 2005. Differential regulation of cortactin and N-WASP-mediated actin polymerization by missing in metastasis (MIM) protein. *Oncogene.* 24:2059–2066.

Loberg, R.D., C.K. Neeley, L.L. Adam-Day, Y. Fridman, L.N. St John, S. Nixdorf, P. Jackson, L.M. Kalikin, and K.J. Pienta. 2005. Differential expression analysis of MIM (MTSS1) splice variants and a functional role of MIM in prostate cancer cell biology. *Int. J. Oncol.* 26:1699–1705.

Mastronarde, D.N. 1997. Dual-axis tomography: an approach with alignment methods that preserve resolution. *J. Struct. Biol.* 120:343–352.

Masuda, M., S. Takeda, M. Sone, T. Ohki, H. Mori, Y. Kamioka, and N. Mochizuki. 2006. Endophilin BAR domain drives membrane curvature by two newly identified structure-based mechanisms. *EMBO J.* 25:2889–2897.

Mattila, P.K., M. Salminen, T. Yamashiro, and P. Lappalainen. 2003. Mouse MIM, a tissue-specific regulator of cytoskeletal dynamics, interacts with ATP-actin monomers through its C-terminal WH2 domain. *J. Biol. Chem.* 278:8452–8459.

Mattila, P.K., O. Quintero-Monzon, J. Kugler, J.B. Moseley, S.C. Almo, P. Lappalainen, and B.L. Goode. 2004. A high-affinity interaction with ADP-actin monomers underlies the mechanism and in vivo function of Srv2/cyclase-associated protein. *Mol. Biol. Cell.* 15:5158–5171.

Miki, H., H. Yamaguchi, S. Suetsugu, and T. Takenawa. 2000. IRSp53 is an essential intermediate between Rac and WAVE in the regulation of membrane ruffling. *Nature.* 408:732–735.

Millard, T.H., G. Bompard, M.Y. Heung, T.R. Dafforn, D.J. Scott, L.M. Machesky, and K. Futterer. 2005. Structural basis of filopodia formation induced by the IRSp53/MIM homology domain of human IRSp53. *EMBO J.* 24:240–250.

Nakagawa, H., H. Miki, M. Nozumi, T. Takenawa, S. Miyamoto, J. Wehland, and J.V. Small. 2003. IRSp53 is colocalised with WAVE2 at the tips of

protruding lamellipodia and filopodia independently of Mena. *J. Cell Sci.* 116:2577–2583.

Palmgren, S., P.J. Ojala, M.A. Wear, J.A. Cooper, and P. Lappalainen. 2001. Interactions with PIP2, ADP-actin monomers, and capping protein regulate the activity and localization of yeast twinfilin. *J. Cell Biol.* 155:251–260.

Papayannopoulos, V., C. Co, K.E. Prehoda, S. Snapper, J. Taunton, and W.A. Lim. 2005. A polybasic motif allows N-WASP to act as a sensor of PIP(2) density. *Mol. Cell.* 17:181–191.

Pardee, J.D., and J.A. Spudich. 1982. Purification of muscle actin. *Methods Enzymol.* 85:164–181.

Peranen, J., M. Rikkonen, M. Hyvonen, and L. Kaariainen. 1996. T7 vectors with modified T7lac promoter for expression of proteins in *Escherichia coli*. *Anal. Biochem.* 236:371–373.

Peter, B.J., H.M. Kent, I.G. Mills, Y. Vallis, P.J. Butler, P.R. Evans, and H.T. McMahon. 2004. BAR domains as sensors of membrane curvature: the amphiphysin BAR structure. *Science.* 303:495–499.

Pollard, T.D., and G.G. Borisy. 2003. Cellular motility driven by assembly and disassembly of actin filaments. *Cell.* 112:453–465.

Qualmann, B., J. Roos, P.J. DiGregorio, and R.B. Kelly. 1999. Syndapin I, a synaptic dynamin-binding protein that associates with the neural Wiskott-Aldrich syndrome protein. *Mol. Biol. Cell.* 10:501–513.

Rameh, L.E., and L.C. Cantley. 1999. The role of phosphoinositide 3-kinase lipid products in cell function. *J. Biol. Chem.* 274:8347–8350.

Salazar, M.A., A.V. Kwiatkowski, L. Pellegrini, G. Cestra, M.H. Butler, K.L. Rossman, D.M. Serna, J. Sondek, F.B. Gertler, and P. De Camilli. 2003. Tuba, a novel protein containing bin/amphiphysin/Rvs and Dbl homology domains, links dynamin to regulation of the actin cytoskeleton. *J. Biol. Chem.* 278:49031–49043.

Suetsugu, S., S. Kurisu, T. Oikawa, D. Yamazaki, A. Oda, and T. Takenawa. 2006a. Optimization of WAVE2 complex-induced actin polymerization by membrane-bound IRSp53, PIP(3), and Rac. *J. Cell Biol.* 173:571–585.

Suetsugu, S., K. Murayama, A. Sakamoto, K. Hanawa-Suetsugu, A. Seto, T. Oikawa, C. Mishima, M. Shirouzu, T. Takenawa, and S. Yokoyama. 2006b. The RAC binding domain/IRSp53-MIM homology domain of IRSp53 induces RAC-dependent membrane deformation. *J. Biol. Chem.* 281:35347–35358.

Takei, K., V.I. Slepnev, V. Haucke, and P. De Camilli. 1999. Functional partnership between amphiphysin and dynamin in clathrin-mediated endocytosis. *Nat. Cell Biol.* 1:33–39.

Tsujita, K., S. Suetsugu, N. Sasaki, M. Furutani, T. Oikawa, and T. Takenawa. 2006. Coordination between the actin cytoskeleton and membrane deformation by a novel membrane tubulation domain of PCH proteins is involved in endocytosis. *J. Cell Biol.* 172:269–279.

Vartiainen, M., P.J. Ojala, P. Auvinen, J. Peranen, and P. Lappalainen. 2000. Mouse A6/twinfilin is an actin monomer-binding protein that localizes to the regions of rapid actin dynamics. *Mol. Cell. Biol.* 20:1772–1783.

Wear, M.A., A. Yamashita, K. Kim, Y. Maeda, and J.A. Cooper. 2003. How capping protein binds the barbed end of the actin filament. *Curr. Biol.* 13:1531–1537.

Woodings, J.A., S.J. Sharp, and L.M. Machesky. 2003. MIM-B, a putative metastasis suppressor protein, binds to actin and to protein tyrosine phosphatase delta. *Biochem. J.* 371:463–471.

Yamagishi, A., M. Masuda, T. Ohki, H. Onishi, and N. Mochizuki. 2004. A novel actin bundling/filopodium-forming domain conserved in insulin receptor tyrosine kinase substrate p53 and missing in metastasis protein. *J. Biol. Chem.* 279:14929–14936.

Young, P., and M. Gautel. 2000. The interaction of titin and alpha-actinin is controlled by a phospholipid-regulated intramolecular pseudoligand mechanism. *EMBO J.* 19:6331–6340.

Zhang, P., and J.E. Hinshaw. 2001. Three-dimensional reconstruction of dynamin in the constricted state. *Nat. Cell Biol.* 3:922–926.